

1 *supporting information to*  
2 **Wind-driven evolution of the North Pacific subpolar gyre over the last**  
3 **deglaciation**

4 William R Gray<sup>1,2\*</sup>, Robert CJ Wills<sup>3</sup>, James WB Rae<sup>2</sup>, Andrea Burke<sup>2</sup>, Ruza F Ivanovic<sup>4</sup>, William HG  
5 Roberts<sup>5</sup>, David Ferreira<sup>6</sup>, Paul J Valdes<sup>7</sup>

6 <sup>1</sup>Laboratoire des Sciences du Climat et de l'Environnement (LSCE/IPSL), Gif-sur-Yvette, France

7 <sup>2</sup>School of Earth and Environmental Science, University of St Andrews, UK

8 <sup>3</sup>Department of Atmospheric Sciences, University of Washington, USA

9 <sup>4</sup>School of Earth & Environment, University of Leeds, UK

10 <sup>5</sup>Geography and Environmental Sciences, Northumbria University, UK

11 <sup>6</sup>Department of Meteorology, University of Reading, UK

12 <sup>7</sup>School of Geographical Sciences, University of Bristol, UK

13

14 \*corresponding author: william.gray@lsce.ipsl.fr

15

16

*Table of contents*

	<i>page</i>
<i>Using planktic foraminiferal <math>\delta^{18}O</math> to trace the gyre boundary</i>	1.
<i>Figure S1</i>	3.
<i>Figure S2</i>	5.
<i>Figure S3</i>	6.
<i>Figure S4</i>	7.
<i>Figure S5</i>	8.
<i>Figure S6</i>	9.
<i>Planktic foraminiferal <math>\delta^{18}O</math> compilation</i>	10.
<i>Figure S7</i>	11.
<i>Seasonality of planktic foraminifera</i>	11.
<i>SST and %Opal data</i>	12.
<i>Figure S8</i>	13.
<i>General circulation models</i>	14.
<i>Figure S9</i>	15.
<i>Eastern boundary test</i>	16.
<i>Figure S10</i>	16.
<i>HSI Freshwater test</i>	16.
<i>Table S1</i>	17.
<i>Table S2</i>	18.

17

18 *Other supporting information not included in this file - Dataset S1*

19

20 *Using planktic foraminiferal  $\delta^{18}O$  to trace the gyre boundary*

21 The  $\delta^{18}O$  of the planktic foraminiferal calcite ( $\delta^{18}O_{\text{calcite}}$ ) is a function of the  $\delta^{18}O$   
22 of seawater ( $\delta^{18}O_{\text{water}}$ , which is closely related to salinity), and the temperature  
23 dependant fractionation between calcite and water ( $\delta^{18}O_{\text{calcite-water}}$ ); specifically, the  
24 fractionation between calcite and water is described by a fractionation factor ( $\alpha_{\text{calcite-}}$

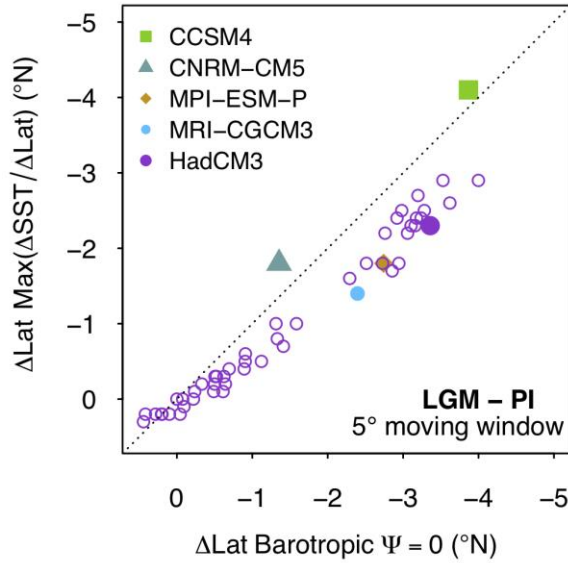
25  $\text{water} = [^{18}\text{O}/^{16}\text{O}]_{\text{calcite}} / [^{18}\text{O}/^{16}\text{O}]_{\text{water}}$  which is related to temperature via,

26 
$$1000 \ln \alpha_{\text{calcite-water}} = 18.03(10^3 T^{-1}) - 32.42$$

27 where T is temperature in Kelvin (Kim and O'Neil, 1997).

28

29 Our ability to use the planktic foraminiferal  $\delta^{18}\text{O}_{\text{calcite}}$  to trace the gyre boundary  
30 comes from the dominance of the temperature signal over that of  $\delta^{18}\text{O}_{\text{water}}$  in driving  
31 the meridional pattern of  $\delta^{18}\text{O}_{\text{calcite}}$  across the basin; the temperature signal is 4-5 times  
32 greater than the  $\delta^{18}\text{O}_{\text{water}}$  signal (Figure 1). As the spatial temperature pattern across the  
33 basin is primarily governed by the gyre circulation, with the steepest meridional  
34 temperature gradient (and thus meridional  $\delta^{18}\text{O}_{\text{calcite}}$  gradient) at the gyre boundary, we  
35 can use the meridional profiles of temperature (and thus  $\delta^{18}\text{O}_{\text{calcite}}$ ) to track the  
36 movement of the gyre boundary. Coupled climate models demonstrate a very tight  
37 coupling between the LGM-PI change in latitude of gyre boundary (defined where  
38 barotropic stream function = 0) and LGM-PI change in the latitude of maximum  
39 latitudinal gradient in sea surface temperature (SST) (Figure S1). As no mechanism  
40 exists to drive changes in  $\delta^{18}\text{O}_{\text{water}}$  of the same magnitude as the changes in  $\delta^{18}\text{O}_{\text{calcite-}}$   
41  $\text{water}$  fractionation from the large temperature difference between the gyres (Figure 1d),  
42 the temperature signal will always dominate over the  $\delta^{18}\text{O}_{\text{water}}$  signal in determining the  
43 spatial pattern of  $\delta^{18}\text{O}_{\text{calcite}}$  (Figure 1e) across the basin and the maximum meridional  
44  $\delta^{18}\text{O}_{\text{calcite}}$  gradient (Figure 1f); thus, while there are likely to be local changes in  $\delta^{18}\text{O}_{\text{water}}$   
45 across the basin, the steepest part of the meridional  $\delta^{18}\text{O}_{\text{calcite}}$  gradient will always be  
46 determined by temperature, allowing us to use meridional profiles of  $\delta^{18}\text{O}_{\text{calcite}}$  to track  
47 the position of the gyre boundary through time.



48

49 **Figure S1** Modelled zonal mean LGM-pre-industrial (PI) change in latitude of gyre boundary (defined  
 50 where barotropic stream function = 0) versus LGM-PI change in latitude of maximum meridional  
 51 gradient in sea surface temperature (SST) within a 5° moving window; the close relationship  
 52 demonstrates past changes in the position of the maximum gradient in SST/Lat (and thus  $\sim\delta^{18}\text{O}_{\text{calcite}}/\text{Lat}$ )  
 53 can be used to trace changes in the position of the gyre boundary.  
 54

55 We model the compiled  $\delta^{18}\text{O}_{\text{calcite}}$  data (see below) as a function of latitude,  
 56 using a Gaussian generalized additive model (GAM) (Wood, 2011; Wood *et al.*, 2016)  
 57 in the *mgcv* package in R (R core Team) at 500 yr timesteps from 18.5 to 10.5 ka (the  
 58 time interval for which we have sufficient spatial and temporal resolution in our dataset;  
 59 Figure 1),

60 
$$\delta^{18}\text{O}_{\text{calcite}} = \beta_0 + f(\text{Lat}) + \varepsilon$$

61 where  $\beta_0$  is the intercept term,  $\varepsilon$  is random error, and  $f(\text{Lat})$  is a smooth function, which  
 62 can be represented as the sum of the underlying basis functions,

63 
$$f(\text{Lat}) = \sum_{j=1}^k b_j(\text{Lat})\beta_j$$

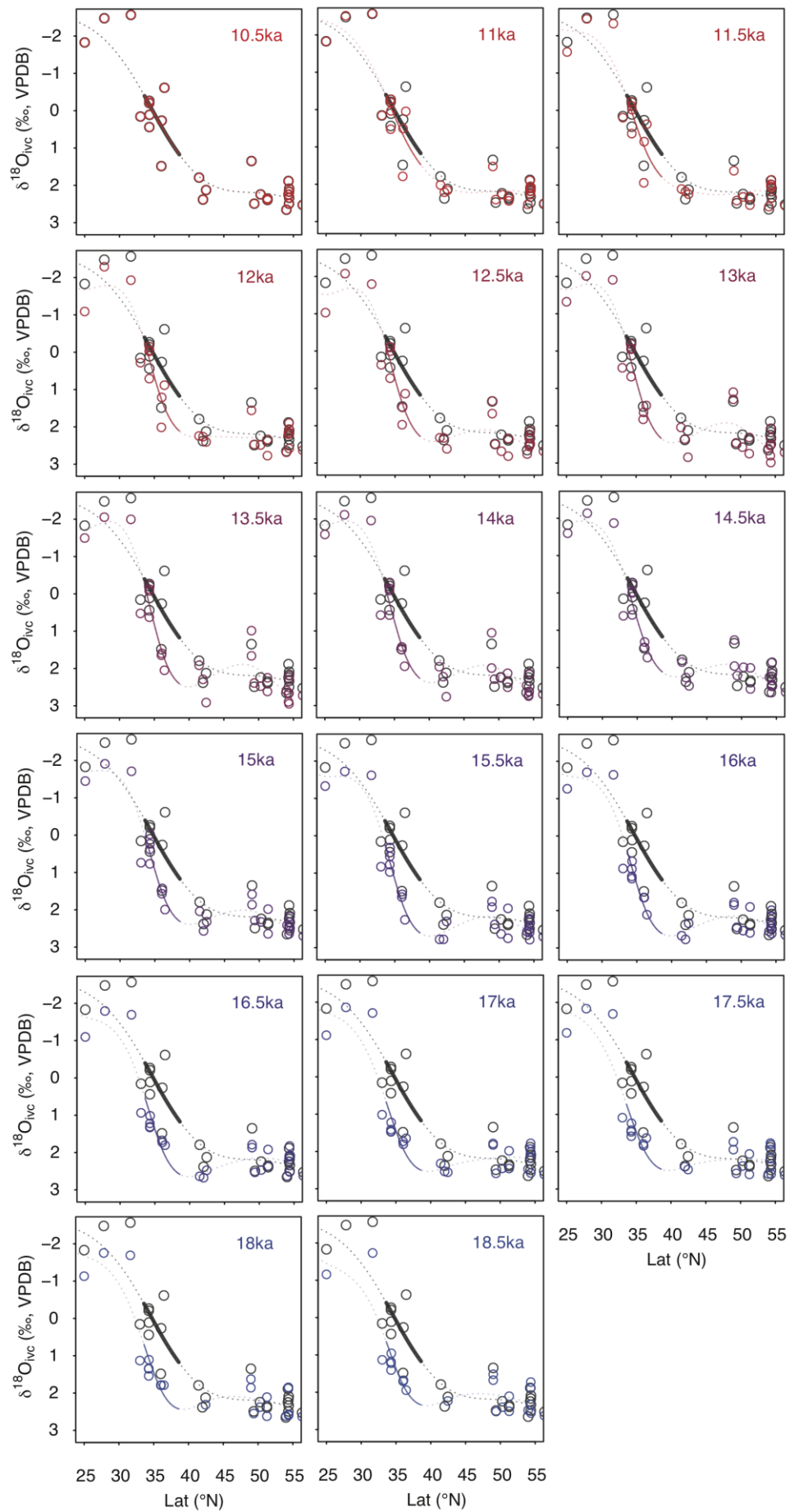
64 where  $b_j$  is the evaluation of the  $j^{\text{th}}$  basis function at the value of Lat, and  $\beta_j$  is the  
 65 estimated coefficient or weight of that basis function. We sum over the weighted values  
 66 of  $k$  basis functions ( $j = 1, 2, \dots, k$ ), which comprise of reduced rank thin plate

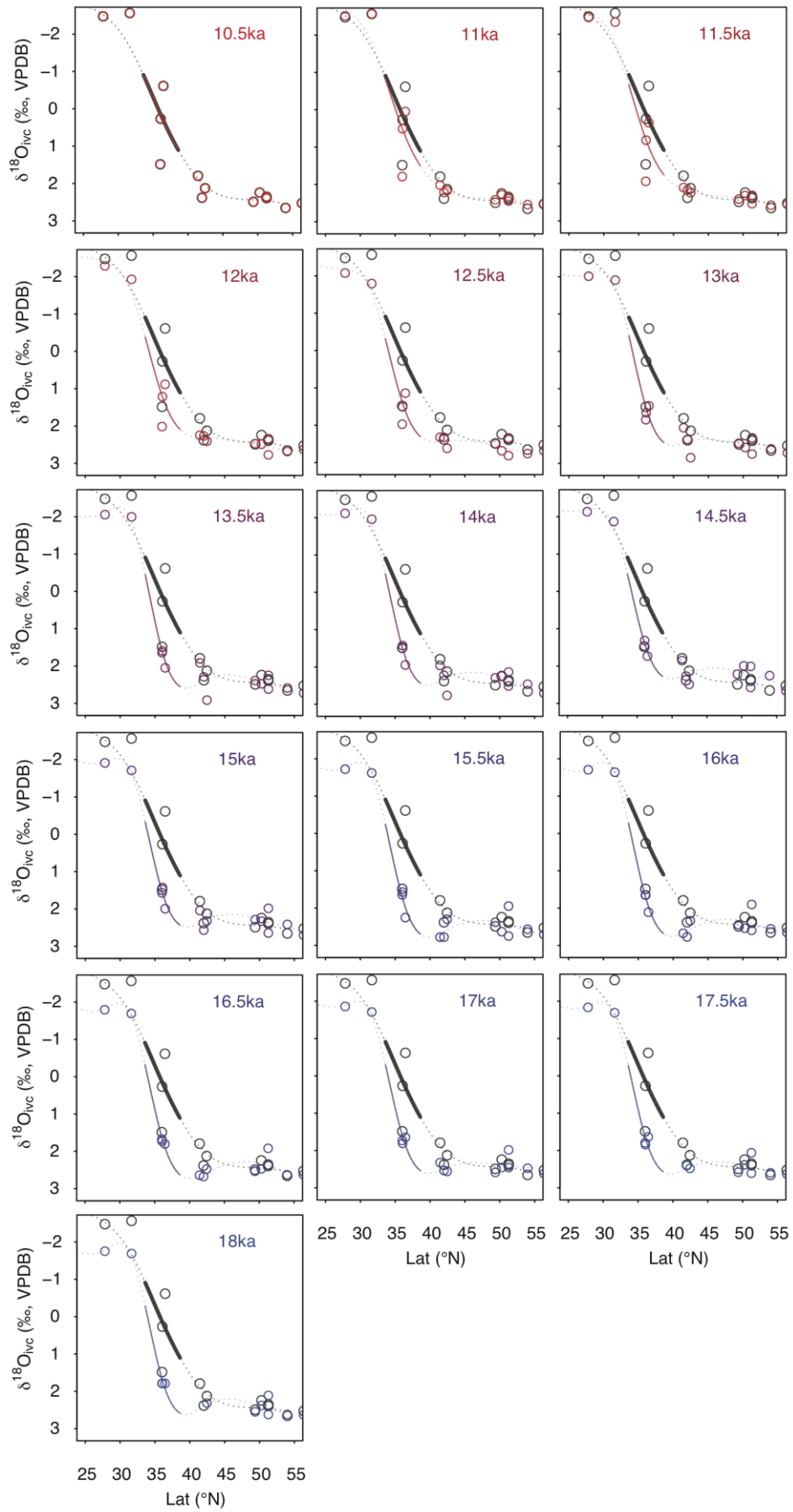
67 regression splines (Wood, 2011; Wood et al., 2016; Simpson, 2018). Here,  $k$  was set to  
68 8, although the value of  $k$  has little effect on the smooth function. The smooth function  
69 is estimated by minimising the penalised sum of squares; the penalty term imposes  
70 smoothness by calculating the integrated square of the second derivative of the spline  
71 (Wood, 2011; Wood et al., 2016; Simpson, 2018),

$$72 \quad \text{penalty} = \lambda \int f''(Lat)^2 dLat$$

73 with the smoothness parameter ( $\lambda$ ) controlling the extent to which the penalty term  
74 contributes to the likelihood of the model, with larger  $\lambda$  giving a smoother function  
75 (Wood, 2011; Wood et al., 2016; Simpson, 2018). The smoothness parameter was  
76 determined using generalised cross validation (GCV). As Restricted Maximum  
77 Likelihood (REML) can sometimes be preferable to GCV as a method to calculate  
78 the smoothing term (Reis and Ogden, 2009; Wood *et al.*, 2016), we tested the models  
79 fitted using GCV by fitting models with an identical form, however using REML to  
80 determine the smoothing term. Both GCV and REML result in identical smoothing  
81 terms, and indistinguishable model fits. Uncertainty envelopes on the fitted models  
82 represent the 68% and 95% Bayesian credible intervals. The reader is directed to  
83 Simpson (2018) for a detailed overview of GAM methodology.

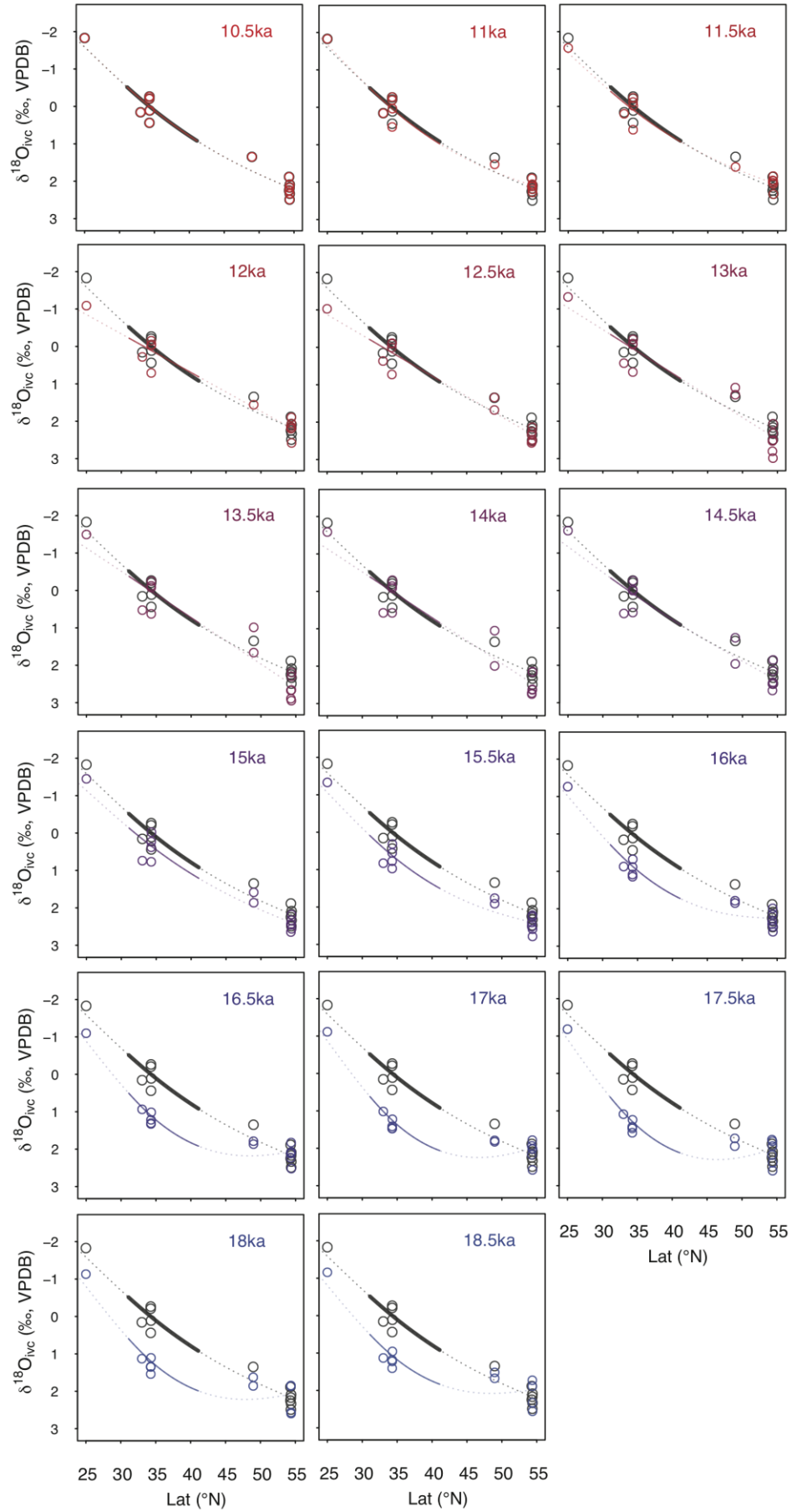
84  
85 **Figure S2 (below)** GAM fits to  $\delta^{18}\text{O}_{\text{calcite}}$  data as a function of latitude at 500 year timesteps from 18.5  
86 to 10.5 ka (colours indicate age); the GAM fit to Holocene  $\delta^{18}\text{O}_{\text{calcite}}$  data (10.5 ka) is shown in dark grey.  
87 The portion of the curve within the latitudinal band used to calculate the shift in gyre position (see Fig.  
88 S5) is shown by the solid line; at each timestep we calculate the latitudinal shift that minimises the  
89 Euclidean distance (along the  $y$ -axis) between the solid part of the coloured curve and the solid part of  
90 the grey curve. Data are the combined east-west dataset (marked ALL on Figure 4).





92  
93

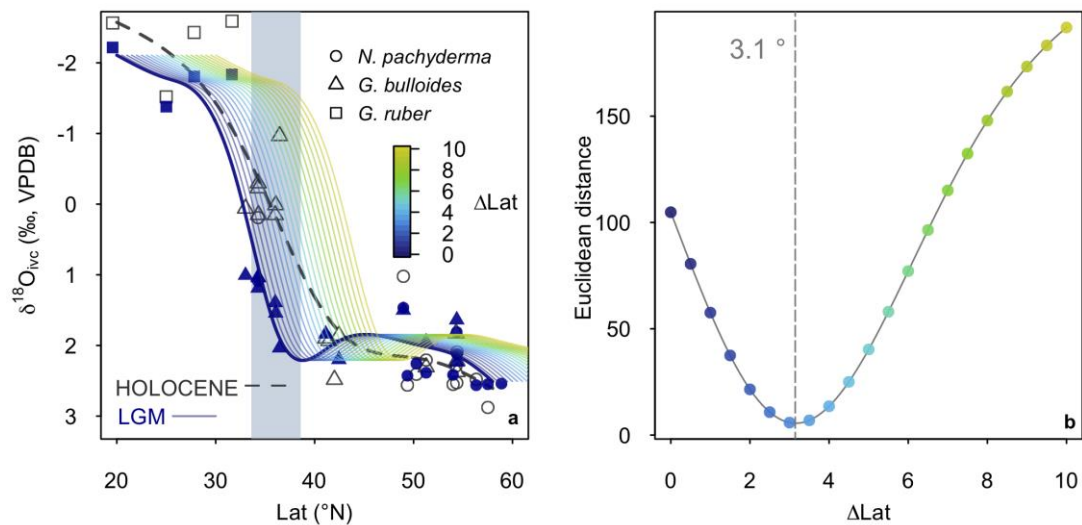
**Figure S3** As figure S2, however data are from west of 180°.



94  
95

**Figure S4** As figure S2, however data are from east of 180°.

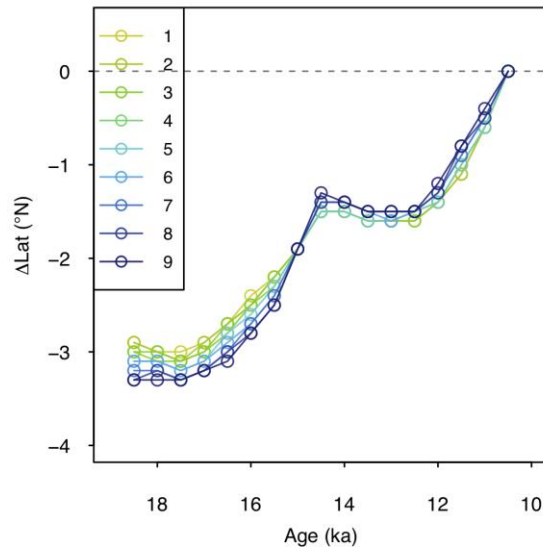
96 We calculate the change in gyre boundary position over deglaciation as the  
 97 latitudinal shift ( $x^\circ$ ) that minimises the Euclidean distance ( $L^2$ ) between the Holocene  
 98 (taken as  $10.5 \pm 0.5$  ka)  $\delta^{18}\text{O}_{\text{calcite}} \sim \text{latitude}$  GAM fit and the GAM fit to each time step,  
 99 within a latitudinal band spanning the gyre boundary; this latitudinal band is centred  
 100 around the maximum gradient in  $\delta^{18}\text{O}_{\text{calcite}}$  versus latitude in the Holocene data within  
 101 a  $5^\circ$  moving window ( $36.1^\circ\text{N}$ ). In the combined dataset from the east and west, and  
 102 the data from the west only, we calculate the latitudinal shift using a  $5^\circ$  latitudinal band  
 103 (i.e.  $33.6$  to  $38.6^\circ\text{N}$ ), and we note the size of this latitudinal band has only a negligible  
 104 effect on our results (Fig. S5); as the gyre boundary (and thus meridional temperature  
 105 and  $\delta^{18}\text{O}_{\text{calcite}}$  gradient) is more diffuse in the east, we use a slightly larger window of  
 106  $10^\circ$  (i.e.  $31.1$  to  $41.1^\circ\text{N}$ ).



107

108 **Figure S5** method used to calculate the shift in gyre boundary position (a) at each time step (here LGM,  
 109 18.5 ka) we calculate the gyre boundary shift as the latitudinal shift ( $x^\circ$ , in  $0.1^\circ$  increments from 0 to 10  
 110 degrees) that minimises the Euclidean distance (b) within a specified latitudinal band (grey box in (a)  
 111 between the GAM fit to the timestep (solid line) and the Holocene (dashed line) in data is calculated.  
 112 The coloured lines in (a) show the LGM GAM fit shifted north in  $0.5^\circ$  increments, and the coloured dots  
 113 in (b) show the Euclidean distance from the Holocene line at each increment, with the colour indicating  
 114 the degree to which the curve has been shifted.  
 115





116

117 **Figure S6 (a)** calculated change in the position of the gyre boundary using different sizes of latitudinal  
 118 band (between 1° and 9°) in which the Euclidean distance between the GAM fits is calculated; the size  
 119 of latitudinal band (the grey box in figure S5a above) has very little effect on the results.  
 120

121 We note that the steepest part of the Holocene curve (~36.1 °N) using the  
 122 combined dataset from the east and west, is further south than the zonal mean position  
 123 of the gyre boundary today (~40 °N). This is due to the westward bias within the dataset  
 124 (i.e. there are many more sites in the west relative to the east within the dataset), and  
 125 the gyre boundary is located slightly further south in the west relative to the zonal mean;  
 126 the maximum meridional gradient in mean annual SST is found at ~36 °N along the  
 127 western margin of the basin (Boyer et al., 2013), in good agreement with our  
 128 reconstruction.

129

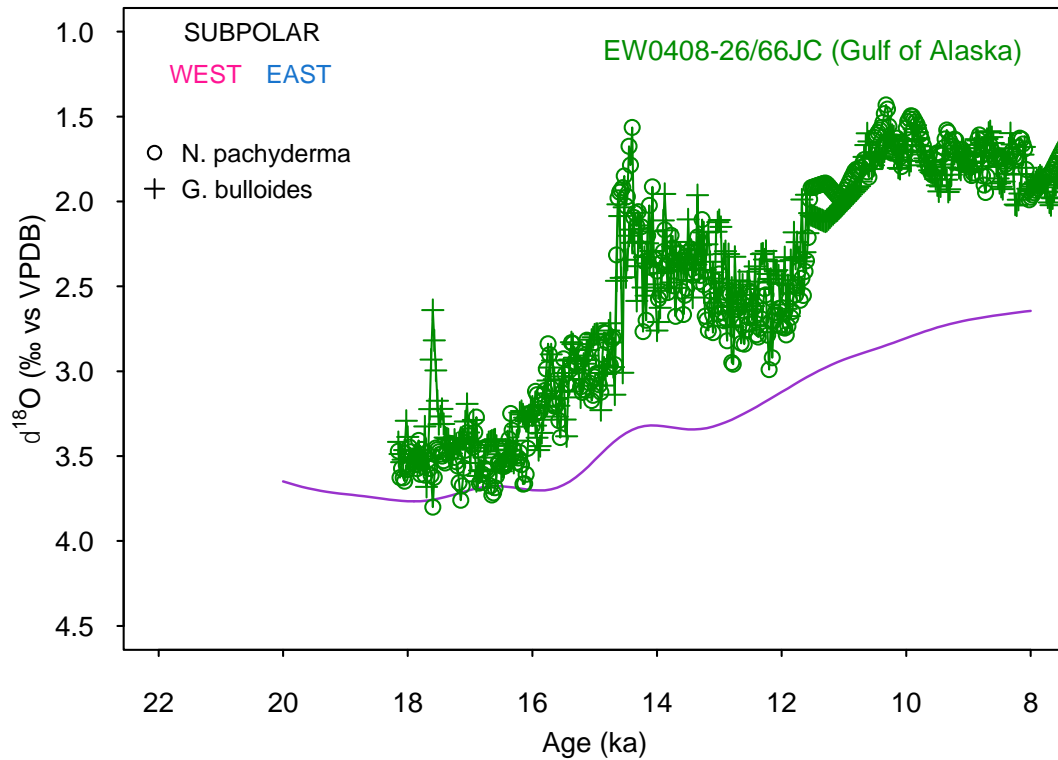
130 We also note that if we use a totally different method to calculate the change in  
 131 position of the gyre boundary, simply calculating the change in latitude in the steepest  
 132 part of the meridional  $\delta^{18}\text{O}_{\text{calcite}}$  gradient (within a 5° moving window), we arrive at a  
 133 very similar estimate of a ~2.6° southward shift between the Holocene and LGM. This  
 134 method is more prone to anomalous values at the latitudinal extremes; hence we opt for  
 135 the method of calculating the latitudinal shift that minimises the Euclidean distance

136 between timesteps within a defined latitudinal band described above. The agreement  
137 between the two methods is, however, reassuring.

138

### 139 *Planktic foraminiferal $\delta^{18}\text{O}_{\text{calcite}}$ compilation*

140 We compiled all available planktic foraminiferal calcite  $\delta^{18}\text{O}$  from cores across the  
141 North Pacific. Compiled records include  $\delta^{18}\text{O}$  measured on *G. ruber*, *G. bulloides*, and  
142 *N. pachyderma*. All data were kept on the original age models, except in the case when  
143 data were only available on uncalibrated  $^{14}\text{C}$  age models, in which case the  $^{14}\text{C}$  data  
144 were recalibrated using INTCAL13 (Reimer et al., 2013) using an average of the  
145 modern reservoir age at each site and a regional glacial increase of +400 years with  
146 large uncertainties ( $\pm 500$  years). All  $\delta^{18}\text{O}_{\text{calcite}}$  data along with the core, location, water  
147 depth, species, sediment depth, age, and original data reference are given in Table S1.  
148 We only include cores spanning the interval between 10.5 to 18.5 ka with an average  
149 resolution of  $>1$  point per ka. We exclude core EW0408-26/66JC from the compilation  
150 (Praetorius and Mix, 2014); this core is located in close proximity to the terminus of  
151 a glacier, and comparing the  $\delta^{18}\text{O}_{\text{calcite}}$  data of this core to other cores within the subpolar  
152 gyre demonstrates planktic foraminiferal  $\delta^{18}\text{O}_{\text{calcite}}$  data from this core primarily reflect  
153 local meltwater changes, rather than wider oceanographic conditions in the subpolar  
154 gyre (Figure S7). The compiled dataset is given in Dataset S1 and will be available on  
155 Pangea.



156

157 **Figure S7** Foraminiferal  $\delta^{18}\text{O}_{\text{calcite}}$  from the subpolar gyre over deglaciation. A GAM fit with to all the  
 158 data (excluding core EW0408-26/66JC) is shown by the purple line, with 68% Bayesian credible interval  
 159 shaded. Data from core EW0408-26/66JC (Praetorius and Mix, 2014) is shown in green.

160

161 *Seasonality of planktic foraminifera*

162 Our approach assumes that any change in seasonal bias relating to the habitat preference

163 of foraminifera are small relative to the change in temperature due to the movement of

164 the gyre boundary. The validity of this approach is supported by sites where  $\delta^{18}\text{O}_{\text{calcite}}$

165 has been measured on more than one species of foraminifera, such as core ODP Site

166 893 or MD02-2489 (Figure 1 and Figure 2). At these sites, foraminiferal species with

167 habitat temperature preferences that are known to be different (*G. bulloides* and *N.*

168 *pachyderma*, e.g. Taylor *et al.*, 2018) show very similar changes down core, with a

169 Holocene-LGM change that is identical (within error); this suggests any changes

170 relating to changes seasonal bias are likely to be insignificant in our reconstruction.

171

172

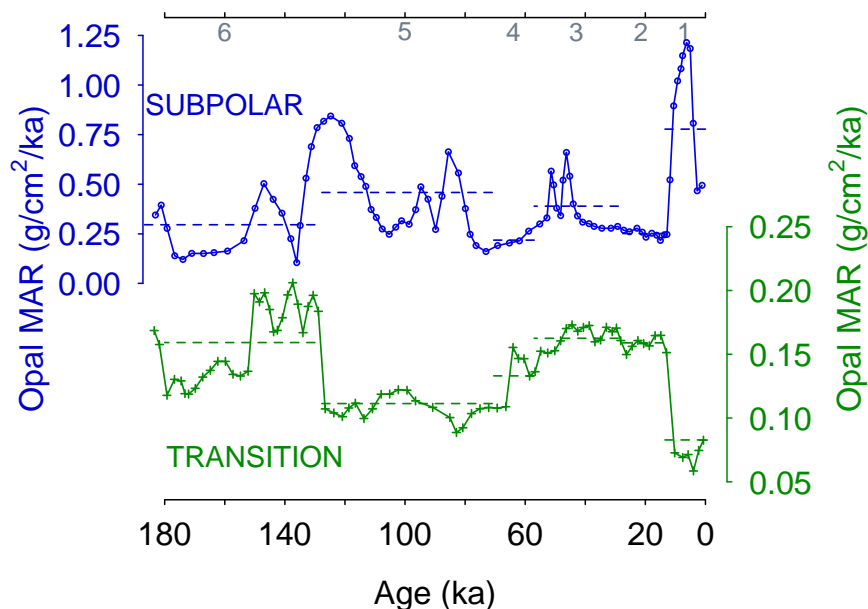
173 *Sea surface temperature and %Opal data*

174 We compiled Mg/Ca and  $U^{K'}_{37}$  sea surface temperature (SST) data from across the  
175 North Pacific (Mg/Ca: Reitdorf et al., 2013; Gebhardt et al., 2008; Rodriguez Sanz et  
176 al., 2013; Taylor et al., 2015; Sagawa et al., 2006; Sagawa et al., 2008; Pak et al., 2012;  
177 Kubota et al., 2010; Gray et al., 2018.  $U^{K'}_{37}$ : Minoshima et al., 2007; Seki, 2004; Harada  
178 et al., 2004; Harada, 2006; Harada et al., 2008; Inagaki et al., 2009; Herbert et al., 2001;  
179 Sawada et al., 1998; Yamamoto et al., 2004; Isono et al., 2009). All age models are as  
180 given in the original publication. All Mg/Ca and  $U^{K'}_{37}$  data were recalibrated (see  
181 below) and the temperature change during the LGM (Figure 2c) is given as a difference  
182 to both proxy temperature in the Holocene, and to mean annual climatological  
183 temperature from the WOA13 (Boyer et al., 2013).

184 While the direct temperature sensitivity of Mg/Ca in planktic foraminifera is ~6% per  
185 °C (Gray et al., 2018b; Gray and Evans, 2019), due to the effect of temperature on pH  
186 through the disassociation constant of water ( $K_w$ ), the ‘apparent’ Mg/Ca temperature  
187 sensitivity is higher (Gray et al., 2018b). Thus, we calculate the change in temperature  
188 from the change in Mg/Ca at each site using a temperature sensitivity of 8.8%, derived  
189 from laboratory cultures (Kisakürek et al., 2008), which encompasses both the direct  
190 temperature effect and the temperature-pH effect, with a Mg/Ca-pH sensitivity of ~ -  
191 8% per 0.1 pH unit (Lea et al., 1999; Russell et al., 2004; Evans et al., 2016; Gray et  
192 al., 2018b; Gray and Evans, 2019). Mg/Ca is also influenced by salinity, with a  
193 sensitivity of ~3-4% per PSU (Hönisch et al., 2013; Gray et al., 2018b; Gray and Evans,  
194 2019). As we are primarily interested in (qualitative) changes in meridional SST  
195 pattern, we make no attempt to account for the whole ocean effects of salinity or pH  
196 downcore. The combined effect of the whole-ocean increase in salinity (due to sea  
197 level), and the increase in surface ocean pH (due to lower atmospheric  $CO_2$ ) means

198 changes in temperature derived from changes in Mg/Ca are likely to be cold-biased by  
 199 ~1.5 °C during the LGM (Gray and Evans, 2019). For  $U^{K'}_{37}$ , the change in temperature  
 200 at each site was calculated using the calibration of Prah1 et al., 1988; the temperature  
 201 range in this study is too low to be substantially effected by the non-linearity of  $U^{K'}_{37}$   
 202 (e.g. Tierney and Tingley, 2018).

203 We analyse the North Pacific %Opal compilation of Kohfeld and Chase (2011)  
 204 to look for qualitative changes in the meridional pattern of productivity over the last  
 205 deglaciation. Due to the high nutrient supply from upwelling, productivity in the SPG  
 206 is an order of magnitude higher than the STG. A southward expansion of the gyre  
 207 boundary should thus result in an increase in productivity within the transition zone;  
 208 transition zone sites show a ~25% increase in %Opal on both sides of the basin during  
 209 the LGM (Figure 2d) consistent with nutrient-rich subpolar waters moving further south  
 210 during the LGM and increasing local productivity.



211

212 **Figure S8** Opal Mass Accumulation Rate data from core KH99-03 in the SPG (Narita et al., 2002) and  
 213 core NCG108 in the transition zone (Maeda et al., 2002). Dashed lines show mean value for each marine  
 214 isotope stage (MIS). Grey shading shows MIS 1, 3 and 5. Transition zone and subpolar waters show an  
 215 anti-phased relationship in Opal MAR over the last glacial cycle.

216 *General Circulation Models*

217         We assess differences in North Pacific barotropic stream function, wind stress  
218 curl, zonal wind stress, and SST between LGM and pre-industrial conditions as  
219 represented by four coupled climate models (CCSM4, CNRM-CM5, MPI-ESM-P and  
220 MRI-CGCM3). All models are part of the Coupled Model Intercomparison Project  
221 phase 5 (CMIP5, Taylor et al., 2012). We only used the four models where both wind  
222 stress and barotropic stream function data are available. Orbital parameters,  
223 atmospheric greenhouse gas concentrations, coastlines and ice topography for the LGM  
224 simulations are standardized as part of the Paleoclimate Model Intercomparison Project  
225 phase 3 (PMIP3) (Braconnot *et al.* 2012, Taylor *et al.* 2012). Ensemble means are  
226 computed by first linearly interpolating to a common grid, and are 4-model means of  
227 100-year climatologies; uncertainties in these centennial averages due to internal  
228 variability are negligible.

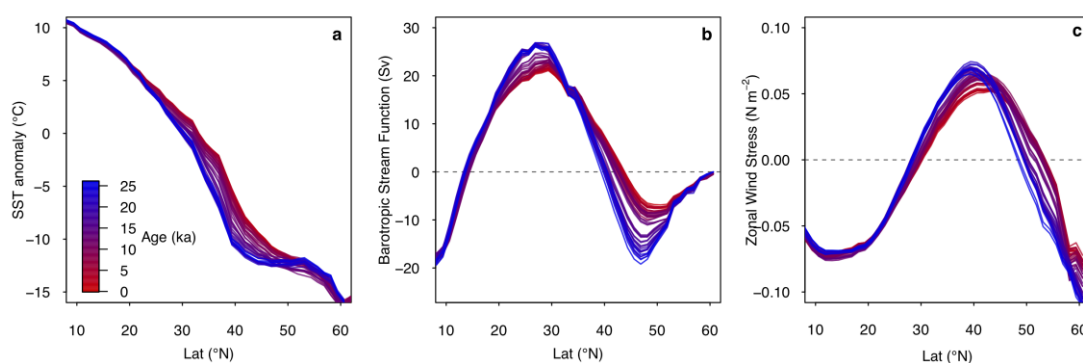
229

230         Using a single model (HadCM3) we look at runs where the model greenhouse  
231 gas, ice sheet albedo, ice sheet topography are changed individually ('Green Mountains,  
232 White Plains') as described in Roberts and Valdes (2017). The 'Green Mountains,  
233 White Plains' runs use the ICE5G ice sheet reconstruction (Peltier *et al.*, 2004), whereas  
234 the deglacial 'snapshot' runs (below) use the ICE6G ice sheet reconstruction (Peltier *et*  
235 *al.*, 2015). The change in gyre boundary position with each forcing are as follows: GHG  
236 = -0.5 °N; Albedo = -0.5 °N; Topography = -0.05 °N; Albedo + Topography = -2.4°N;  
237 ALL (although with the smaller ICE6G ice sheet) = -3.4 °N.

238

239         We also explore changes through time over the deglaciation using a series of  
240 HadCM3 equilibrium-type simulations where all forcings and model boundary

241 conditions are changed at 500-year intervals broadly adhering to the PMIP4 last  
 242 deglaciation protocol (Ivanovic et al., 2016). These simulations use the ICE6GC ice  
 243 sheet reconstruction and 'melt-uniform' scenario for ice sheet meltwater; i.e. freshwater  
 244 from the melting ice sheets is NOT routed to the ocean via coastal outlets. Instead,  
 245 water is conserved by forcing the global mean ocean salinity to be consistent with the  
 246 change in global ice sheet volume with respect to present. Note, these deglacial  
 247 simulations are not transient, but are equilibrium-type experiments that begin from the  
 248 end of the 1750-year long simulations run by Singarayer et al. (2011). At each 500-year  
 249 interval (21.0 ka, 20.5 ka, 20.0 ka...0.5 ka, 0.0 ka), all boundary conditions and forcings  
 250 are updated according to the more recent literature (presented by Ivanovic et al., 2016)  
 251 and held constant for the full 500-year duration of the run. The climate means and  
 252 standard deviations used here are calculated from the last 50 years of each simulation  
 253 (i.e. year 451-500, inclusive). More information on these runs can be found in the  
 254 supplement to Morris et al. (2018), noting that we use the raw model output and not the  
 255 downscaled and bias-corrected data used in the previous publication. Zonal mean  
 256 changes in SST anomaly (from global mean), barotropic stream function, and zonal  
 257 wind stress at each time step are shown below (Fig. S9).



258

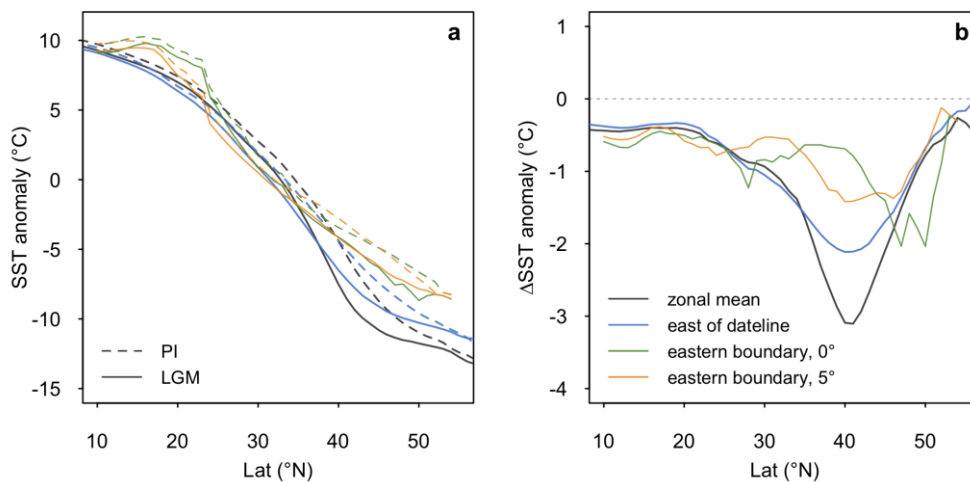
259 **Figure S9** Deglacial evolution of zonal mean (a) SST anomaly (relative to global mean) (b) barotropic  
 260 stream function (c) zonal wind stress in the HadCM3 simulations.

261

262

263 *Eastern boundary test*

264 To test if there is an influence of coastal upwelling on the data in the east (i.e. a signal  
265 of some other control on latitudinal temperature anomaly [and thus latitudinal  $\delta^{18}\text{O}_{\text{calcite}}$   
266 anomaly] besides change in gyre position) we compare the ensemble mean SST along  
267 the eastern boundary of the basin (taken as the first oceanic grid point west of land  
268 during the LGM) to the zonal mean, and zonal mean east of the dateline (Fig. S10).  
269 The models show no indication of a strong influence of coastal upwelling, which would  
270 manifest as an anomalous cooling relative to the zonal mean. This analysis suggests  
271 coastal upwelling is unlikely to be having a significant effect on our results, although  
272 the simulated coastal upwelling may be poorly represented due to the resolution of the  
273 models.



274

275 **Figure S10 (a)** LGM and PI SST anomaly (from global mean), and **(b)** LGM-PI SST anomaly in different  
276 longitudinal bins; zonal mean (grey), zonal mean east of the dateline (180°, blue), along the eastern  
277 boundary of the basin (green), and 5° seaward from the eastern boundary of the basin (orange). Note, the  
278 gyre boundary is located slightly further north along the eastern margin relative to the zonal mean and  
279 zonal mean east of the dateline.  
280

281 *HSI Freshwater test*

282 The release of large amounts of freshwater into the eastern subpolar North Pacific has  
283 been suggested over deglaciation, at ~17.5 ka (Maier *et al* 2018). The release of  
284 freshwater into the eastern subpolar North Pacific is evident in an increase in the



285  $\delta^{18}\text{O}_{\text{calcite}}$  difference between the mixed-layer dwelling species *G. bulloides* and the  
286 slightly deeper-dwelling species *N. pachyderma* in core MD02-2489 (54.39°N, -  
287 148.92°E ) at this time; during this interval *G. bulloides* becomes ~0.6 ‰ more depleted  
288 than *N. pachyderma*. To test if this release of freshwater may be influencing our gyre  
289 boundary reconstruction we re-run the gyre-boundary analysis, however removing the  
290 *G. bulloides* data from core MD02-2489; the results are identical to the gyre boundary  
291 reconstruction including the *G. bulloides* data demonstrating that the effect of  
292 freshwater release has very little effect on our gyre boundary reconstruction. This is  
293 because the change in  $\delta^{18}\text{O}_{\text{calcite}}$  from the freshwater release (~0.6 ‰, equivalent to ~2  
294 PSU freshening) is very small compared to the large change in  $\delta^{18}\text{O}_{\text{calcite}}$  resulting from  
295 the temperature difference between the gyres (~5.5 ‰). Localised freshwater inputs,  
296 while having a large effect locally, do very little to change the pattern of  $\delta^{18}\text{O}_{\text{calcite}}$  at  
297 the basin scale.

298

299

300

301

302

303

304

305

306

307

308

309

310

311

**Table S1** Compiled planktic foraminiferal  $\delta^{18}\text{O}_{\text{calcite}}$  records. The compiled will be made available on Pangea.

Core	Lat (°N)	Lon (°E)	Species	Reference
MD02-2489	54.39	-148.921	<i>N. pachyderma</i>	Gebhardt et al 2008
MD02-2489	54.39	-148.921	<i>G. bulloides</i>	Gebhardt et al 2008
PAR87A-10	54.363	-148.4667	<i>G. bulloides</i>	Zahn et al 1991
PAR87A-10	54.363	-148.4667	<i>N. pachyderma</i>	Zahn et al 1991
PAR87A-02	54.29	-149.605	<i>G. bulloides</i>	Zahn et al 1991
PAR87A-02	54.29	-149.605	<i>N. pachyderma</i>	Zahn et al 1991
MD02-2496	48.967	-127.033	<i>N. pachyderma</i>	Taylor et al 2015
MD02-2496	48.967	-127.033	<i>G. bulloides</i>	Taylor et al 2015
ODP1017	34.32	-121.6	<i>G. bulloides</i>	Pak et al 2012
ODP893	34.2875	-120.03667	<i>N. pachyderma</i>	Hendy et al 2002
ODP893	34.2875	-120.03667	<i>G. bulloides</i>	Hendy et al 2002
MD02-2503	34.28	-120.04	<i>G. bulloides</i>	Hill et al 2006
AHF-28181	33.011667	-119.06	<i>G. bulloides</i>	Mortyn et al 1996
MD05-2505	25	-112	<i>G. ruber</i>	Rodríguez-Sanz et al 2013
SO201-2-101	58.883	170.683	<i>N. pachyderma</i>	Reitdorf et al 2013
SO201-2-85	57.505	170.413167	<i>N. pachyderma</i>	Reitdorf et al 2013
SO201-2-77	56.33	170.69883	<i>N. pachyderma</i>	Reitdorf et al 2013
SO201-2-12	53.992667	162.375833	<i>N. pachyderma</i>	Reitdorf et al 2013
MD01-2416	51.268	167.725	<i>N. pachyderma</i>	Gebhardt et al 2008
MD01-2416	51.268	167.725	<i>G. bulloides</i>	Gebhardt et al 2008
VINO-GGC37	50.28	167.7	<i>N. pachyderma</i>	Keigwin 1998
LV29-114-3	49.375667	152.877933	<i>N. pachyderma</i>	Reitdorf et al 2013
KT90-9_21	42.45	144.3167	<i>G. bulloides</i>	Oba and Murayama 2004
GH02-1030	42	144	<i>G. bulloides</i>	Sagawa and Ikehara 2008
CH84-14	41.44	142.33	<i>G. bulloides</i>	Labeyrie 1996
CH84-04	36.46	142.13	<i>G. bulloides</i>	Labeyrie 1996
MD01-2420	36.067	141.817	<i>G. bulloides</i>	Sagawa et al 2006
MD01-2421	36.01667	141.7833	<i>G. bulloides</i>	Oba and Murayama 2004
KY07_04_01	31.6391667	128.944	<i>G. ruber</i>	Kubota et al 2010
A7	27.82	126.98	<i>G. ruber</i>	Sun et al 2005
ODP184-1145	19.58	117.63	<i>G. ruber</i>	Oppo and Sun 2005

312

313

314

315

316

317

318

**Table S2** Reconstructed change in gyre boundary latitude (°N). Uncertainty is 1 $\sigma$ .

age	DLat	DLat_error	DLat_west	DLat_west_error	Dlat_east	DLat_east_error
10.5	0.0	0.9	0.0	1.0	0	1.2
11.0	-0.6	0.8	-0.7	0.9	-0.3	1.1
11.5	-1.0	0.8	-1.1	0.9	-0.5	1.2
12.0	-1.4	0.7	-1.7	0.8	-0.5	1.2
12.5	-1.5	0.7	-1.9	0.8	-0.8	1.1
13.0	-1.6	0.7	-1.8	0.8	-0.2	1.3
13.5	-1.6	0.7	-1.8	0.8	0	1.3
14.0	-1.5	0.7	-1.7	0.8	0.2	1.3
14.5	-1.5	0.7	-1.7	0.8	-0.5	1.5
15.0	-1.9	0.7	-1.9	0.8	-2.4	1.3
15.5	-2.3	0.7	-2.1	0.8	-3.9	1.2
16.0	-2.6	0.7	-2.1	0.7	-5	1.2
16.5	-2.8	0.8	-2.0	0.7	-5.9	1.1
17.0	-3.1	0.8	-2.0	0.7	-6.3	1.2
17.5	-3.2	0.8	-2.0	0.7	-6.3	1.3
18.0	-3.1	0.8	-2.0	0.7	-6.4	1.4
18.5	-3.1	0.8	NA	NA	-6	1.5

Age is in ka

DLat is change in gyre boundary position (°N) using all data

DLat\_west is change in gyre boundary position (°N) using data west of 180°

DLat\_east is change in gyre boundary position (°N) using data east of 180°

Uncertainty is 1 $\sigma$  – see methods for details.

319

**320 Additional References**

- 321 Boyer, T.P., Antonov, J.I., Baranova, O.K., Coleman, C., Garcia, H.E., Grodsky, A., John-  
322 son, D.R., Locarnini, R.A., Mishonov, A.V., O'Brien, T.D., Paver, C.R., Reagan, J.R., Seidov, D., Smolyar, I.V., Zweng, M.M., 2013.  
323 World Ocean Database 2013. In: Levitus, Sydney (Ed.), Alexey Mishonov (Technical Ed.), NOAA Atlas  
324 NESDIS, vol. 72. 209 pp.
- 325 Evans D., Wade B. S., Henahan M., Erez J. and Müller W. (2016) Revisiting carbonate chemistry controls on  
326 planktic foraminifera Mg / Ca: Implications for sea surface temperature and hydrology shifts over the Paleocene-  
327 Eocene Thermal Maximum and Eocene-Oligocene transition. *Clim. Past* 12.
- 328 Gebhardt, H. et al., Paleonutrient and productivity records from the subarctic North Pacific for Pleistocene glacial  
329 terminations I to V. *Paleoceanography* 23, PA4212 (2008).
- 330 Gray, W. R., Weldeab, S., Lea, D. W., Rosenthal, Y., Gruber, N., Donner, B. and Fischer, G. (2018b) The effects of  
331 temperature, salinity, and the carbonate system on Mg/Ca in *Globigerinoides ruber* (white): A global sediment  
332 trap calibration. *Earth Planet. Sci. Lett.* 482, 607–620.
- 333 Gray, W.R. and Evans, D. (2019) Nonthermal influences on Mg/Ca in planktonic foraminifera: A review of culture  
334 studies and application to the last glacial maximum. *Paleoceanography and Paleoclimatology*, 34. <https://doi.org/10.1029/2018PA003517>
- 335
- 336 Harada, N. Ahagon, N., Uchida, M. (2004) Northward and southward migrations of frontal zones during the past 40  
337 kyr in the Kuroshio-Oyashio transition area. *Geochemistry*, doi:10.1029/2004GC000740/pdf.
- 338 Harada, N. (2006) Rapid fluctuation of alkenone temperature in the southwestern Okhotsk Sea during the past 120  
339 ky. *Global and Planetary Change*. 53, 29–46.
- 340 Harada, N., Sato, M., Sakamoto, T. (2008) Freshwater impacts recorded in tetraunsaturated alkenones and alkenone  
341 sea surface temperatures from the Okhotsk Sea across millennial-scale cycles. *Paleoceanography*. 23, PA3201.
- 342 Harada, N., Sato, M., Sakamoto, T. (2008) Freshwater impacts recorded in tetraunsaturated alkenones and alkenone  
343 sea surface temperatures from the Okhotsk Sea across millennial-scale cycles. *Paleoceanography*. 23, PA3201.

344 Hendy, I. L., Kennett, J. P., Roark, E. B., Ingram, B. L., (2002) Apparent synchronicity of submillennial scale climate  
345 events between Greenland and Santa Barbara Basin, California from 30-10 ka. *Quaternary Science Reviews* 21,  
346 1167-1184.

347 Herbert, D. et al. (2001) Collapse of the California Current During Glacial Maxima Linked to Climate Change on  
348 Land. *Science*. 293, 71–76.

349 Hill, T.M., J.P. Kennett, D.K. Pak, R.J. Behl, C. Robert, and L. Beaufort. 2006. Pre-Bolling warming in Santa  
350 Barbara Basin, California: surface and intermediate water records of early deglacial warmth. *Quaternary Science*  
351 *Reviews* 25, pp. 2835–2845, doi:10.1016/j.quascirev.2006.03.012

352 Hönisch B., Allen K. a., Lea D. W., Spero H. J., Eggins S. M., Arbuszewski J., deMenocal P., Rosenthal Y., Russell  
353 A. D. and Elderfield H. (2013) The influence of salinity on Mg/Ca in planktic foraminifers – Evidence from  
354 cultures, core-top sediments and complementary  $\delta^{18}\text{O}$ . *Geochim. Cosmochim. Acta* 121, 196–213.

355 Inagaki, M., Yamamoto, M., Igarashi, Y., Ikehara, K. (2009) Biomarker records from core GH02-1030 off Tokachi  
356 in the northwestern Pacific over the last 23,000 years: Environmental changes during the last deglaciation.  
357 *Journal of Oceanography*. 65, 847–858.

358 Isono, D. et al. (2009) The 1500-year climate oscillation in the midlatitude North Pacific during the Holocene.  
359 *Geology*. 37, 591–594.

360 Kisakürek, B., Eisenhauer, A., Böhm, F., Garbe-Schönberg, D., Erez, J., 2008. Controls on shell Mg/Ca and Sr/Ca  
361 in cultured planktonic foraminiferan, *Globigerinoides ruber* (white). *Earth Planet. Sci. Lett.* 273, 260–269.  
362 <https://doi.org/10.1016/j.epsl.2008.06.026>.

363 Kubota, Y., K. Kimoto, R. Tada, H. Oda, Y. Yokoyama, and H. Matsuzaki (2010), Variations of East Asian summer  
364 monsoon since the last deglaciation based on Mg/Ca and oxygen isotope of planktic foraminifera in the northern  
365 East China Sea, *Paleoceanography*, 25, PA4205, doi:10.1029/2009PA001891.

366 Labeyrie, L. 1996. Quaternary paleoceanography: unpublished stable isotope records. IGBP PAGES/World Data  
367 Center for Paleoclimatology Data Contribution Series #1996-036. NOAA/NGDC Paleoclimatology Program,  
368 Boulder, Colorado, USA.

369 Lea D. W., Mashiotta T. A. and Spero H. J. (1999) Controls on magnesium and strontium uptake in planktonic  
370 foraminifera determined by live culturing. *Geochim. Cosmochim. Acta* 63, 2369–2379.

371 Maeda, L., H. Kawahata and M. Noharta (2002): Fluctuation of biogenic and abiogenic sedimentation on the Shatsky  
372 Rise in the western north Pacific during the late Quaternary. *Marine Geology* 189, 197-214.

373 Minoshima, K., H. Kawahata, K. Ikehara (2007) Changes in biological production in the mixed water region (MWR)  
374 of the northwestern North Pacific during the last 27 kyr. *Palaeogeography, Palaeoclimatology, Palaeoecology*.  
375 254, 430–447.

376 Mortyn, P. G., Thunell, R. C., Anderson, D. M., Stott, L. D., Le, J. (1996) Sea surface temperature changes in the  
377 Southern California Borderlands during the last glacial-interglacial cycle. *Paleoceanography* 11, 415-430.

378 Narita, H., M. Sato, S. Tsunogai, M. Maruyama, M. Ikehara, T. Nkatsuka, M. Wakatsuchi, N. Harada and U. Ujiie  
379 (2002): Biogenic opal indicating less productive northwestern North Pacific during glacial stages. *Geophys. Res.*  
380 *Lett.*, 29(15), 22-1 to 22-4.

381 Oba, T., Murayama, M. (2004) Sea-surface temperature and salinity changes in the northwest Pacific since the Last  
382 Glacial Maximum. *Journal of Quaternary Science* 19, 335-346.

383 Oppo, D. W., and Y. Sun (2005) Amplitude and timing of sea surface temperature change in the northern South  
384 China Sea: Dynamic link to the East Asian monsoon. *Geology* 33, 785–788.

385 Pak, D. K., D. W. Lea, and J. P. Kennett (2012) Millennial scale changes in sea surface temperature and ocean  
386 circulation in the northeast Pacific, 10–60 kyr BP, *Paleoceanography* 27, PA1212, doi:10.1029/2011PA002238.

387 Peltier, W. R. (2004). Global glacial isostasy and the surface of the Ice-Age Earth: The ICE-5G (VM2) model and  
388 GRACE. *Annual Review of Earth and Planetary Sciences*, 32(1), 111–149.  
389 <https://doi.org/10.1146/annurev.earth.32.082503.144359>

390 Praetorius, S. K., Mix, A. C. (2014) Synchronization of North Pacific and Greenland climates preceded abrupt  
391 deglacial warming. *Science* 345, 444. DOI: 10.1126/science.1252000.

392 Prah, F. G., L. A. Muehlhausen, and D. L. Zahnle (1988), Further evaluation of long-chain alkenones as indicators  
393 of paleoceanographic conditions, *Geochim. Cosmochim. Acta* 52, 2303–2310.

394 Reimer, P. J. et al. (2013) IntCal13 and Marine13 radiocarbon age calibration curves 0-50,000 years cal BP.  
395 *Radiocarbon* 55, 1869–1887.

396 Reiss, P. T., Ogden, R. T. (2009) Smoothing parameter selection for a class of semiparametric linear models. *Journal*  
397 *of the Royal Statistical Society B* 71, 505-523.

398 Riethdorf, J.-R., Max, L., Nürnberg, D., Lembke-Jene, L., Tiedemann, R. (2013) Deglacial development of (sub)  
399 sea surface temperature and salinity in the subarctic northwest Pacific: Implications for upper-ocean  
400 stratification. *Paleoceanography*. 28, 91–104.

401 Rodríguez Sanz, L., Mortyn, P. G., Herguera, J. C., Zahn, R. (2013) Hydrographic changes in the tropical and  
402 extratropical Pacific during the last deglaciation. *Paleoceanography*. 28, 529–538.  
403 Russell A. D., Hönisch B., Spero H. J. and Lea D. W. (2004) Effects of seawater carbonate ion concentration and  
404 temperature on shell U, Mg, and Sr in cultured planktonic foraminifera. *Geochim. Cosmochim. Acta* 68, 4347–  
405 4361.  
406 Sagawa, T., Toyoda, K., Oba, T. (2006) Sea surface temperature record off central Japan since the Last Glacial  
407 Maximum using planktonic foraminiferal Mg/Ca thermometry.  
408 Sagawa, T., Ikehara, K. (2008) Intermediate water ventilation change in the subarctic northwest Pacific during the  
409 last deglaciation. *Geophysical Research Letters* 35, L24702, doi:10.1029/2008GL035133.  
410 Seki, O., et al. (2004) Reconstruction of paleoproductivity in the Sea of Okhotsk over the last 30 kyr.  
411 *Paleoceanography*. 19, PA1016.  
412 Singarayer, J.S., Valdes, P.J., Friedlingstein, P., Nelson, S., Beerling, D.J., 2011. Late Holocene methane rise caused  
413 by orbitally controlled increase in tropical sources. *Nature* 470, 8285. <https://doi.org/10.1038/nature09739>  
414 Taylor, B.J., Rae, J.W.B., Gray, W.R., Darling, K.F., Burke, A., Gersonde, R., Abelman, A., Maier, E., Esper, O.,  
415 Ziveri, P. (2018) Distribution and ecology of planktic foraminifera in the North Pacific: Implications for paleo-  
416 reconstructions. *Quaternary Science Reviews* 191, 256-274.  
417 Taylor, M. A., Hendy, I. L., Pak, D. K. (2014) Deglacial ocean warming and marine margin retreat of the Cordilleran  
418 Ice Sheet in the North Pacific Ocean. *Earth and Planetary Science Letters*. 403, 89–98 (2014).  
419 Tierney J. E. and Tingley M. P. (2018) BAYSPLINE: A New Calibration for the Alkenone Paleothermometer.  
420 *Paleoceanogr. Paleoclimatology* 33, 281–301.  
421 Yamamoto, M., Oba, T., Shimamune, J., Ueshima, T. (2004) Orbital-scale anti-phase variation of sea surface  
422 temperature in mid-latitude North Pacific margins during the last 145,000 years. *Geophysical Research Letters*.  
423 31, L16311.  
424 Zahn, R., Pedersen, T. F., Bornhold, B. D., Mix, A. C. (1991) Watermass conversion in the glacial subarctic Pacific  
425 (54°N, 148°W): physical constraints and the benthic-planktonic stable isotope record. *Paleoceanography* 6, 543-  
426 560.